One-dimensional proximity superconductivity in the quantum Hall regime

https://doi.org/10.1038/s41586-024-07271-w

Received: 24 October 2023

Accepted: 5 March 2024

Published online: 24 April 2024



Check for updates

Julien Barrier^{1,2, Minsoo} Kim^{1,3}, Roshan Krishna Kumar⁴, Na Xin^{1,5, M}, P. Kumaravadivel^{1,2}, Lee Hague², E. Nguyen^{1,2}, A. I. Berdyugin^{1,2}, Christian Moulsdale^{1,2}, V. V. Enaldiev^{1,2}, J. R. Prance⁶, F. H. L. Koppens⁴, R. V. Gorbachev^{1,2}, K. Watanabe⁷, T. Taniguchi⁷, L. I. Glazman⁸, I. V. Grigorieva^{1,2}, V. I. Fal'ko^{1,2,9} & A. K. Geim^{1,2⊠}

Extensive efforts have been undertaken to combine superconductivity and the quantum Hall effect so that Cooper-pair transport between superconducting electrodes in Josephson junctions is mediated by one-dimensional edge states $^{1-6}$. This interest has been motivated by prospects of finding new physics, including topologically protected quasiparticles⁷⁻⁹, but also extends into metrology and device applications^{10–13}. So far it has proven challenging to achieve detectable supercurrents through quantum Hall conductors^{2,3,6}. Here we show that domain walls in minimally twisted bilayer graphene 14-18 support exceptionally robust proximity superconductivity in the quantum Hall regime, allowing Josephson junctions to operate in fields close to the upper critical field of superconducting electrodes. The critical current is found to be non-oscillatory and practically unchanging over the entire range of quantizing fields, with its value being limited by the quantum conductance of ballistic, strictly one-dimensional, electronic channels residing within the domain walls. The system described is unique in its ability to support Andreev bound states at quantizing fields and offers many interesting directions for further exploration.

Proximity superconductivity based on quasi-one-dimensional conductors acting as weak links has attracted considerable interest from both fundamental and applied perspectives. It leads to phenomena involving magnetic flux tunnelling^{10,19}, and there is the associated prospect of the ampere standard being based on quantum phase slips 11-13. In terms of applications, the critical current I_c in Josephson junctions is normally suppressed by very weak perpendicular magnetic fields B because of Fraunhofer-type interference between Cooper pairs propagating along different trajectories²⁰. If proximity superconductivity were provided by strictly one-dimensional states, the suppression could be avoided, allowing superconducting quantum interference devices to operate at high B. Of particular interest is the use of the quantum Hall conductors as weak links because this not only allows control of the mediating one-dimensional states by a gate voltage but also can lead to the realization of topologically protected many-body quasiparticles (see, for example, refs. 8,9). Despite the long-term interest in Josephson junctions incorporating quantum Hall conductors, the experimental progress has so far been limited mainly to observations of the influence of superconducting electrodes on normal-state transport and studies of so-called chiral Andreev edge states that appear at superconductor-quantum Hall conductor interfaces 1-6,21,22. Recently, proximity superconductivity in the quantum Hall regime has been reported for graphene-based Josephson junctions^{2,6,22}. Supercurrents supported by quantum Hall edge states were found to be extremely fragile (critical current $I_c \approx 1$ nA at millikelvin temperatures^{2,6,22,23}), so that often the proximity cannot be reproduced even for devices with conceptually similar designs^{20,24,25}. Below, we describe an alternative route for achieving superconducting coupling deep in the quantum Hall regime. It utilizes boundaries between AB and BA domains in Bernal-stacked bilayer graphene^{14–18,26–30}, which are found to serve as ballistic, strictly one-dimensional wires connecting superconducting electrodes in quantizing B where the graphene bulk becomes completely insulating for Cooper pairs.

The devices studied were made from minimally twisted graphene bilayers (MTGBs), as detailed in Methods. In brief, monolayer graphene was cut into two pieces that were then placed on top of each other using a parallel transfer accompanied by rotation at an angle of less than 0.1° ('Device fabrication' in Methods). Such an assembly is known to undergo lattice reconstruction, which results in the formation of relatively large regions of Bernal-stacked bilayer graphene. These regions are separated by narrow AB/BA domain walls with a width $w \approx 10$ nm (refs. 14,15). The resulting domain structures can be visualized by piezo-force microscopy (Extended Data Fig. 1a), and, for MTGBs fully encapsulated in hexagonal boron nitride (Methods), by photocurrent scanning microscopy (Extended Data Fig. 1b,c). Electron-beam lithography, dry etching and thin-film deposition were employed to make superconductor-normal metal-superconductor junctions with MTGBs playing the role of the normal metal between superconducting (NbTi) electrodes separated by distances $L \approx 100-200$ nm (Methods). The electrodes have a critical temperature $T_c \approx 7.0$ K and an upper critical

Department of Physics and Astronomy, University of Manchester, Manchester, UK. 2National Graphene Institute, University of Manchester, Manchester, UK. 3Department of Applied Physics, Kyung Hee University, Yong-in, South Korea. 4ICFO — Institut de Ciencies Fotoniques, The Barcelona Institute of Science and Technology, Castelldefels, Barcelona, Spain. 5Department of Chemistry, Zhejiang University, Hangzhou, China. Department of Physics, Lancaster University, Lancaster, UK. National Institute for Materials Science, Tsukuba, Japan. Department of Physics, Yale University, New Haven, CT, USA. 9Henry Royce Institute for Advanced Materials, University of Manchester, Manchester, UK. e-mail: julien.barrier@icfo.eu; na.xin@zju.edu.cn; geim@manchester.ac.uk

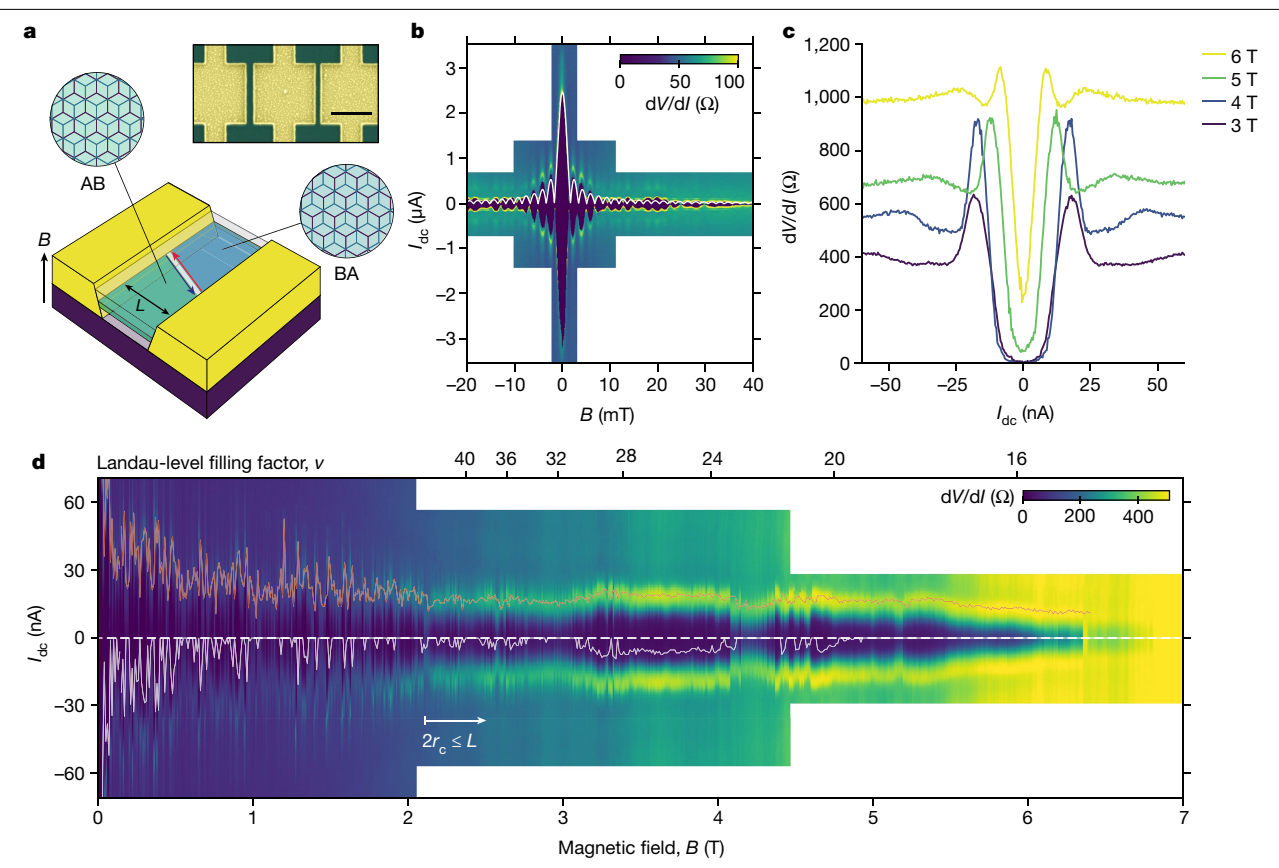


Fig. 1|Josephson junctions incorporating domain walls in MTGBs. a, Device schematic showing a domain wall acting as a weak link in the quantum Hall regime. Regions with AB and BA stacking are illustrated by the circular insets. The carrier density was varied by applying gate voltage to a Si wafer shown in dark blue (Methods). Top inset, false-colour electron micrograph of a typical device containing several edgeless Josephson junctions in series. MTGB is shown in green, and NbTi in yellow. Scale bar, 1 µm. b, Differential resistance as

a function of I_{dc} at small B for a junction with a single domain wall. Strong deviations from the Fraunhofer pattern (white curve) emerge above 10 mT. \mathbf{c} , Examples of dV/dI curves in the quantum Hall regime for the same junction. \mathbf{d} , Full map measured up to 7 T in steps of 10 mT. The red curve shows I_{c} defined as peak positions in dV/dI (I_{dc}). The white curve marks the zero-resistance state boundary where a finite V emerged above the noise level. Data in $\mathbf{b} - \mathbf{d}$ are for the same edged junction: $W \approx 3 \ \mu\text{m}$, $L \approx 200 \ \text{nm}$, $n \approx 2 \times 10^{12} \ \text{cm}^{-2}$, 50 mK and $I_{ac} = 3 \ \text{nA}$.

field $H_{c2} \approx 9.5$ T. Eight devices were studied, each containing three to seven MTGB junctions (Fig. 1a and Extended Data Fig. 1d,e). The junctions' widths W were between 0.5 and 4 μ m, and they incorporated different numbers of domain walls $N_{\rm DW}$ to act as weak links between the NbTi electrodes (Fig. 1a). Josephson junctions were made in two geometries that we refer to as edged and edgeless, such that the graphene was either etched away everywhere except for a narrow slit between the electrodes or extended well beyond it, respectively (schematics in Fig. 1a and Extended Data Fig. 1f). Comparisons between the two geometries allowed us to assess the role played by graphene edges. As a reference, we also made similar Josephson junctions but without domain walls ($N_{\rm DW} = 0$) as well as Josephson junctions incorporating extended defects (slits and wrinkles) connecting the NbTi electrodes ('Josephson junctions without domain walls' in Methods).

In addition to the imaging, we employed normal-state electron transport to evaluate $N_{\rm DW}$ within the examined Josephson junctions. To this end, the two-probe conductance was measured at the neutrality point for high B (filling factor v=0). For Josephson junctions without domain walls, their neutrality-point conductance approached zero, indicating that the MTGB bulk became insulating at v=0 (Extended Data Fig. 2). In contrast, devices with domain walls exhibited a finite zero-v conductance with values weakly dependent on T and close to $4e^2/h$ per domain wall, where e is the electron charge and h the Planck constant (Extended Data Fig. 2d). This observation agrees with the theoretical expectation that, at the neutrality point, AB/BA walls should support chiral spin-degenerate edge states 17,18,29,30 . Good correlation was found

between $N_{\rm DW}$ estimated from our imaging and zero- ν measurements (Extended Data Fig. 2b). Because domain walls can shift and even disappear from Josephson junctions during fabrication (Methods) and because their number is difficult to identify from images if the domain walls are too close to each other, below we label Josephson junctions according to the $N_{\rm DW}$ values found from the transport measurements.

To characterize Josephson junctions in the superconducting state, we measured their IV characteristics using small a.c. currents I_{ac} of typically 2–5 nA and varying d.c. bias I_{dc} ('Characterization of MTGB junctions' in Methods). First, we focus on the behaviour of Josephson junctions at high gate-induced electron densities (positive $n > 10^{12}$ cm⁻²), which provided a low-resistance normal metal-superconductor interface between MTGBs and NbTi electrodes (approximately 10 Ω μ m). At low $B \lesssim 50$ mT, all our devices exhibited similar characteristics, independent of N_{DW} and their design (including the reference Josephson junctions). The examples in Fig. 1b and Extended Data Fig. 3a show differential resistance dV/dI maps around zero B. They are dominated by the expected interference (Fraunhofer) oscillations, although deviations from the standard dependence (white curves) are also notable. Such behaviour is typical for graphene Josephson junctions^{20,25}. At intermediate B (before entering the quantum Hall regime), $I_c(B)$ did not decay proportionally to 1/B, as expected for conventional superconductor-normal metal-superconductor junctions, but instead exhibited giant fluctuations with numerous pockets of the zeroresistance state, which persisted up to a few tesla in our shortest junctions (Fig. 1d and Extended Data Fig. 4). This 'mesoscopic' behaviour

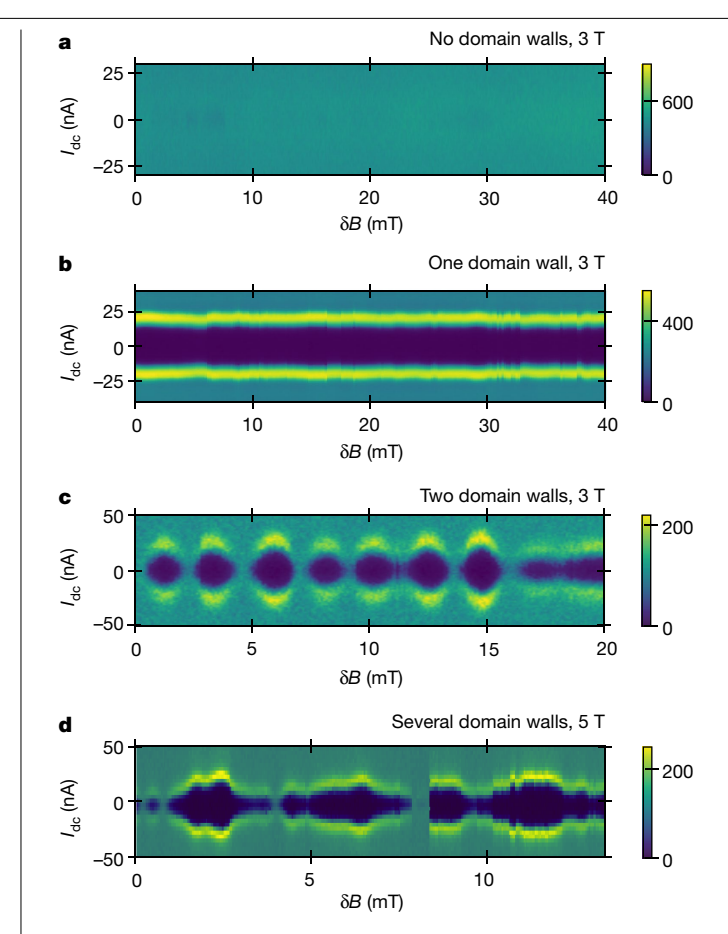


Fig. 2 | Supercurrent in the quantum Hall regime for different numbers of domain walls. a-d, Differential resistance maps for Josephson junctions without domain walls (a) or with one domain wall (b), two domain walls (c) and 14 ± 4 domain walls (d). All devices were electron doped with $n \approx 2-3 \times 10^{12}$ cm⁻². B was varied in steps of approximately 50 μ T for $T \approx 50$ mK and $I_{ac} = 5$ nA. Colour scales in ohms. $\mathbf{a} - \mathbf{c}$ were measured at B = 3 T and \mathbf{d} at 5 T.

is characteristic of ballistic Josephson junctions²⁰ and, again, was observed for all our devices. Both the low- and intermediate-B regimes have been discussed in detail previously^{20,25} and are briefly reviewed in Methods. Accordingly, our emphasis below is on the proximity superconductivity that emerged in the quantum Hall regime and was exclusive to Josephson junctions containing domain walls.

From the semiclassical perspective, ballistic junctions enter the quantum Hall regime if the cyclotron diameter $2r_c$ becomes smaller than L so that only skipping orbits along edges (or domain walls) connect the superconducting electrodes directly. In the normal state, the onset of the quantum Hall regime was evident as a rapid increase of the two-probe resistance and the concurrent appearance of Shubnikovde Haas (SdH) oscillations (Extended Data Figs. 2a, 5 and 10a). In this regime, no supercurrent could be discerned in any Josephson junction without domain walls, neither for the edged nor edgeless geometry, nor in reference devices (Fig. 2a and Extended Data Fig. 5), and not even in Josephson junctions incorporating the narrow slits (less than 10 nm) that supported closely spaced counterpropagating edge states (Extended Data Fig. 5c and 'Josephson junctions without domain walls' in Methods). This agrees with the previous reports^{20,23-25}, especially when taking into account our highly transparent, normal metal-superconductor interfaces such that chiral Andreev edge states are expected to decohere at short distances⁶. In stark contrast, every Josephson junction with domain walls exhibited proximity superconductivity that extended deep into the quantum Hall regime (Fig. 1c,d and Extended Data Fig. 3b) and could approach H_{c2} within approximately

1T (Extended Data Fig. 4b). This shows that domain walls provide an exceptionally robust channel for Cooper-pair transport. Comparing Josephson junctions with different $N_{\rm DW}$, we found that each domain wall could typically carry a supercurrent of approximately 10 nA (Extended Data Figs. 3 and 8). To emphasize the robustness and reproducibility of the domain wall-supported proximity, we also studied the inverse a.c. Josephson effect (Shapiro steps) in the quantum Hall regime and found good agreement between the experiment and theory (Extended Data Fig. 9).

Looking in more detail, for Josephson junctions with a single domain wall, the proximity superconductivity not only persisted deep into the quantum Hall regime but also exhibited a qualitative change in behaviour such that, counterintuitively, supercurrents appeared to be stabilized by quantizing fields. Indeed, giant fluctuations in $I_c(B)$. characteristic of intermediate B, were suppressed for $2r_c \lesssim L$, where $I_{\rm c}$ remained constant over extended field intervals of approximately 0.1 T (Fig. 2b and Extended Data Fig. 6b,c). This is in contrast to $2r_c > L$, where the superconductivity was confined to millitesla-scale pockets²⁰ (Fig. 1d). Furthermore, I_c varied relatively little over the entire interval of quantizing B (despite strong and oscillating changes in the normal-state resistance) and disappeared only on approach to H_{c2} . On top of this gradual variation, we observed numerous abrupt changes, mostly small but occasionally substantial in magnitude (Fig. 1d and Extended Data Fig. 7). They were irreproducible for different sweeps of B and different sweep directions (Extended Data Fig. 7) and attributed to jumps of pinned vortices in the NbTi electrodes. This is generally expected because Andreev bound states responsible for Josephson coupling should depend on the superconducting order parameter in the vicinity of domain walls and, hence, local vortex configurations^{5,21}.

For Josephson junctions with several domain walls, the behaviour $could also \, be \, understood \, from \, the \, same \, perspective. \, For \, two \, domain \,$ walls, the supercurrent was approximately twice as high as for one domain wall and showed oscillations nearly periodic in B (Fig. 2c), as expected for interference between constant supercurrents carried by two channels. The observed periodicity in B was a few times longer than that for the Fraunhofer oscillations near zero B, which yielded that, in the quantum Hall regime, the characteristic area per flux quantum $\phi_0 = h/2e$ was smaller than the total Josephson junction area $L \times W$, in agreement with two supercurrent channels being present within the junction. For many domain walls, the oscillating pattern became aperiodic and was interrupted more frequently by vortex jumps (Fig. 2d and Extended Data Fig. 4b). This agrees with the presence of several supercurrent channels, which should result in a convoluted interference pattern that is further complicated by vortices intervening at many locations.

The most revealing feature of the behaviour observed for single-domain wall junctions is minimal variations in I_c over a wide range of B. If the supercurrent were due to Andreev bound states arising from quantum Hall states counterpropagating at the opposite sides of the domain wall, one would expect Aharonov-Bohm oscillations with a periodicity $\Delta B \approx \phi_0/(w + 2r_c)L < 0.1$ T, where $2r_c$ accounts for the extent of quantum Hall edge states into the graphene bulk ('Steady supercurrent along a single domain wall' in Methods). No sign of such oscillatory behaviour was observed in our Josephson junctions (Figs. 1d and 2b and Extended Data Figs. 6 and 7). Even including vortex jumps, $I_c(B)$ in the quantum Hall regime varied by less than a third over intervals of more than 3 T (Fig. 2d), which ruled out any underlying oscillations with ΔB < 10 T. The latter value translates into a spatial scale $\phi_0/\Delta BL\lesssim 1$ nm, much less than even the superconducting coherence length in NbTi. This means that quantum Hall edge states could not be responsible for the observed proximity. This is also consistent with that our slits with a width of less than 10 nm supported no supercurrent in the quantum Hall regime, despite the nearby counterpropagating edge states. To explain why $I_c(B)$ remained steady over several tesla, we refer to recent calculations that suggested the presence of non-chiral one-dimensional

channels inside domain walls²⁹, which differ from the well-known one-dimensional states that appear if an energy gap is opened in the graphene bulk ^{17,18,26-28}. These internal channels are valley degenerate so that Andreev bound states involving the one-dimensional electrons do not encircle any magnetic flux. This explains the constant $I_c(B)$, such as shown in Fig. 2b and Extended Data Fig. 6b,c. The remaining variations in supercurrent over larger B intervals can be attributed to a gradual suppression of the order parameter as vortices jump and pack up at the normal metal–superconductor interface.

The magnitude of the supercurrents observed in the quantum Hall regime (up to 20 nA per domain wall) is also revealing. At zero B, the $I_c(T)$ dependence (Extended Data Fig. 8a) was exponential with characteristic energy $\delta E \approx 0.2$ meV (for details, see Methods). This suggests that our ballistic losephson junctions were in the long-junction regime where the supercurrent was limited by decoherence of Andreev bound states rather than the superconducting gap, in agreement with previous conclusions for ballistic two-dimensional junctions^{20,31,32}. The value of I_c at zero B is described well by $\delta E/eR_n$ where R_n is the normal-state resistance of the Josephson junctions. This is, again, in agreement with refs. 20,31. It is reasonable to expect that the decoherence should be equally important for our one-dimensional channels of the same length L. Therefore, roughly the same δE limited the critical current along domain walls. This reasoning is consistent with the T dependence observed in the quantum Hall regime (Extended Data Fig. 8c). Although R_n for the discussed range of high B and n was, typically, approximately $0.5 \text{ k}\Omega$ (Fig. 2), this value arises mostly due to bulk carriers²⁰. The supercurrent itself was provided by domain walls and should then be limited by their resistance, that is, by $h/4e^2$ (only a single one-dimensional sub-band is expected to be occupied²⁹; Extended Data Fig. 2d). Accordingly, we expect $I_c \approx (\delta E/e)/(h/4e^2) \approx 30$ nA. This agrees well with the experiment, especially considering an additional contact resistance at the one-dimensional-three-dimensional interface between the domain wall and NbTi electrodes, which should reduce Ic.

Finally, we discuss how the one-dimensional proximity superconductivity was affected by the carrier density n. At low B, the n dependences were similar for all our Josephson junctions, with or without domain walls (Fig. 3a). In comparison to the previous reports using Josephson junctions made from monolayer graphene^{20,25}, the only notable difference was the near absence of Fabry-Pérot oscillations in our devices. Such oscillations require a limited transparency of the normal metal-superconductor interface to allow standing waves and were previously observed for hole doping for which interfacial pn junctions provided suitable conditions^{20,25}. The two-dimensionalthree-dimensional interface for our bilayer Josephson junctions was quite transparent, even with hole doping, and caused only weak Fabry-Pérot oscillations near zero B (Fig. 3a). In the quantum Hall regime, the normal metal-superconductor interface changed its character into one-dimensional-three-dimensional and no supercurrent could be detected for hole doping because of the high resistance of the interfacial pn junctions (Fig. 3b). On the other hand, pronounced oscillations in $I_c(n)$ were observed for electron doping as the one-dimensionalthree-dimensional interface was more transparent. These oscillations are attributed to Fabry-Pérot resonances that occur each time an integer number of half the one-dimensional Fermi wavelength matches the domain wall length L (Fig. 3b and Extended Data Fig. 10). A surprising feature of the observed Fabry-Pérot oscillations was that their period changed little with decreasing *n*, even when approaching the neutrality point (Fig. 3b,c). This behaviour is described in detail in Methods and seems difficult to reconcile with that the electron wavelength generally diverges at zero carrier density. Nonetheless, the observed periodicity is in good quantitative agreement with that expected for our specific one-dimensional channels (Fig. 3c) in which electrons inside the domain walls retain a finite density even for charge-neutral bilayers²⁹ (Supplementary Information).

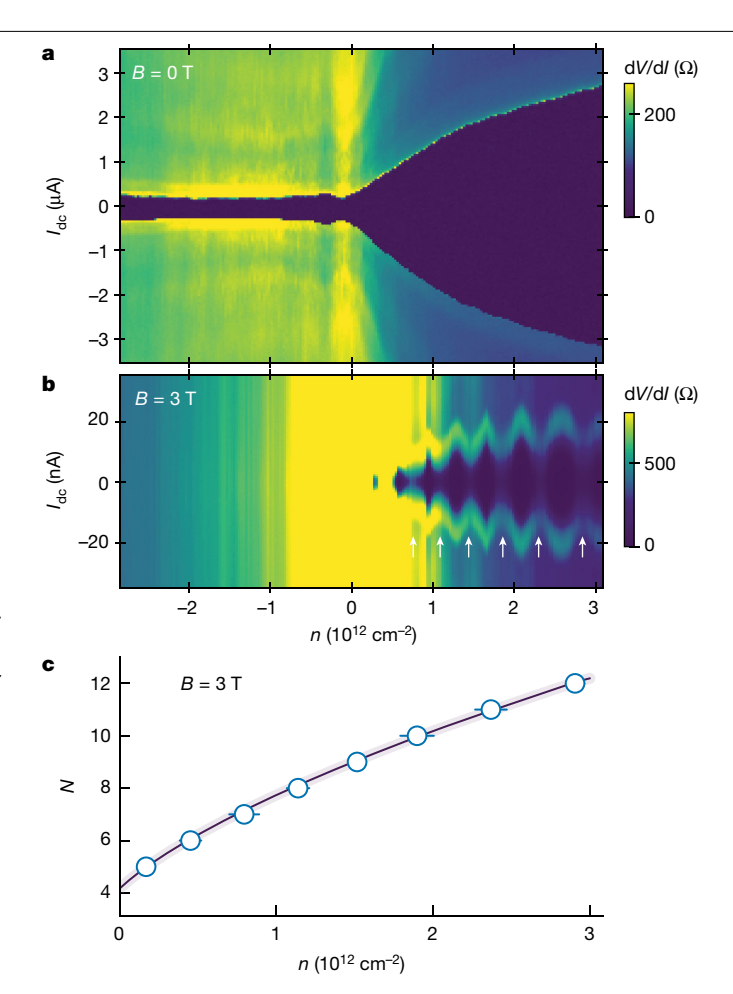


Fig. 3 | **Fabry-Pérot oscillations in the supercurrent provided by a single domain wall. a,b**, Differential resistance as a function of doping and d.c. bias for zero field (**a**) and the quantum Hall regime (**b**). In **b**, B = 3 T corresponds to $2r_c < L$ for all n. Positive and negative n correspond to electron and hole doping, respectively. Same Josephson junction as in Fig. 1 for $T \approx 50$ mK and $I_{ac} = 5$ nA. White arrows in **b** indicate minima in I_c . **c**, Positions of observed minima in terms of n (symbols) compared with the expected Fabry-Pérot resonances for one-dimensional electrons inside a 10-nm-wide domain wall with L = 160 nm (solid curve). For details, see Methods and Supplementary Information. Horizontal error bars indicate the uncertainty in determining the positions of the minima (Extended Data Fig. 10).

To conclude, AB/BA domain walls are unique in their ability to support Andreev bound states in the quantum Hall regime. The walls allow high critical currents reaching near the theoretical limit and are practically independent of B due to the strictly one-dimensional nature of the electronic states inside the walls. This ballistic system offers many interesting directions for further exploration. For example, if the energy gap is opened in the bilayer graphene bulk by biasing the two layers¹⁷, the one-dimensional states inside AB/BA domain walls acquire topological protection²⁹ and should allow chiral supercurrents³⁻⁶, which is an essential albeit not sufficient condition for the realization of non-abelian anyons^{5,33}. It would also be interesting to see how the observed proximity superconductivity is affected if the spin or valley degeneracy is lifted by exchange interactions, which may, for example, allow tunable π junctions. Furthermore, because the one-dimensional Andreev bound states are tunnel-coupled to the graphene bulk, there is an intriguing possibility of exploring the interactions of the supercurrents with fractional and, especially, even-denominator quantum Hall states that have been observed in encapsulated bilayer graphene and have been suggested to contain non-abelian quasiparticles⁸. Finally,

AB/BA domain walls provide interesting venues not only within the physics of low-dimensional superconductivity but also in terms of normal-state transport due to their unusually long, wire-like geometry while preserving ballistic properties. Such one-dimensional systems are exceptionally rare and could be used to address a number of phenomena in one dimension, including Luttinger liquids.

Note added in proof: After the manuscript was accepted, a series of papers was brought to our attention, including refs. 34,35. They report proximity superconductivity in 3D bismuth nanowires in high magnetic fields and attribute it to chiral surface states. Although not directly related to the subject of our report (superconductivity in the quantum Hall regime), the work can be of interest for experts working on topologically protected quasiparticles and Josephson junctions in general.

Online content

Any methods, additional references, Nature Portfolio reporting summaries, source data, extended data, supplementary information, acknowledgements, peer review information; details of author contributions and competing interests; and statements of data and code availability are available at https://doi.org/10.1038/s41586-024-07271-w.

- Eroms, J., Weiss, D., De Boeck, J., Borghs, G. & Zülicke, U. Andreev reflection at high magnetic fields: evidence for electron and hole transport in edge states, Phys. Rev. Lett. 95 107001 (2005)
- Amet, F. et al. Supercurrent in the quantum Hall regime, Science 352, 966-969 (2016).
- Lee, G.-H. et al. Inducing superconducting correlation in quantum Hall edge states Nat. Phys. 13, 693-698 (2017)
- Sahu, M. R. et al. Inter-Landau-level Andreev reflection at the Dirac point in a graphene quantum Hall state coupled to a NbSe₂ superconductor. Phys. Rev. Lett. 121, 086809 (2018).
- Zhao, L. et al. Interference of chiral Andreev edge states. Nat. Phys. 16, 862-867 (2020).
- Vignaud, H. et al. Evidence for chiral supercurrent in quantum Hall Josephson junctions. Nature 624, 545-550 (2023).
- Bretheau, L. et al. Exciting Andreev pairs in a superconducting atomic contact, Nature 499, 312-315 (2013).
- Alicea, J. New directions in the pursuit of Majorana fermions in solid state systems Rep. Prog. Phys. 75, 076501 (2012).
- Lutchyn, R. M. et al. Majorana zero modes in superconductor-semiconductor heterostructures. Nat. Rev. Mater. 3, 52-68 (2018).
- Bezryadin, A., Lau, C. N. & Tinkham, M. Quantum suppression of superconductivity in ultrathin nanowires. Nature 404, 971-974 (2000).
- 11. Mooij, J. E. & Nazarov, Y. V. Superconducting nanowires as quantum phase-slip junctions. Nat. Phys. 2, 169-172 (2006).
- Astafiev, O. V. et al. Coherent quantum phase slip. Nature 484, 355-358 (2012).
- Shaikhaidarov, R. S. et al. Quantized current steps due to the ac coherent quantum phase-slip effect, Nature 608, 45-49 (2022).

- Huang, S. et al. Topologically protected helical states in minimally twisted bilayer graphene. Phys. Rev. Lett. 121, 037702 (2018).
- Yoo, H. et al. Atomic and electronic reconstruction at the van der Waals interface in twisted bilayer graphene. Nat. Mater. 18, 448-453 (2019).
- San-Jose, P. & Prada, E. Helical networks in twisted bilayer graphene under interlayer bias. Phys. Rev. B 88, 121408 (2013).
- Ju, L. et al. Topological valley transport at bilayer graphene domain walls. Nature 520, 650-655 (2015).
- Alden, J. S. et al. Strain solitons and topological defects in bilayer graphene. Proc. Natl Acad. Sci. USA 110, 11256-11260 (2013).
- Lau, C. N., Markovic, N., Bockrath, M., Bezryadin, A. & Tinkham, M. Quantum phase slips in superconducting nanowires. Phys. Rev. Lett. 87, 217003 (2001).
- Ben Shalom, M. et al. Quantum oscillations of the critical current and high-field superconducting proximity in ballistic graphene, Nat. Phys. 12, 318-322 (2016).
- Wei, M. T. et al. Chiral quasiparticle tunneling between quantum Hall edges in proximity with a superconductor. Phys. Rev. B 100, 121403 (2019).
- 22. Seredinski, A. et al. Quantum Hall-based superconducting interference device. Sci. Adv. 5, eaaw8693 (2019).
- Seredinski, A. et al. Supercurrent in graphene Josephson junctions with narrow trenches in the quantum Hall regime. MRS Adv. 3, 2855-2864 (2018).
- Indolese. D. I. et al. Compact SQUID realized in a double-layer graphene heterostructure. Nano Lett. 20, 7129-7135 (2020).
- Calado, V. E. et al. Ballistic Josephson junctions in edge-contacted graphene. Nat. Nanotech. 10, 761-764 (2015).
- 26. Efimkin, D. K. & MacDonald, A. H. Helical network model for twisted bilayer graphene. Phys. Rev. B 98, 035404 (2018).
- Rickhaus, P. et al. Transport through a network of topological channels in twisted bilayer graphene. Nano Lett. 18, 6725-6730 (2018).
- Xu, S. G. et al. Giant oscillations in a triangular network of one-dimensional states in marginally twisted graphene. Nat. Commun. 10, 4008 (2019).
- Enaldiev, V. V., Moulsdale, C., Geim, A. K. & Fal'ko, V. I. Non-chiral one-dimensional sates propagating inside AB/BA domain walls in bilayer graphene. Preprint at arxiv.org/abs/ 2307.14293 (2023).
- Geisenhof, F. R. et al. Interplay between topological valley and quantum Hall edge transport. Nat. Commun. 13, 4187 (2022).
- Borzenets, I. V. et al. Ballistic graphene Josephson junctions from the short to the long junction regimes. Phys. Rev. Lett. 117, 237002 (2016).
- Bardeen, J. & Johnson, J. L. Josephson current flow in pure superconducting-normal-superconducting junctions. Phys. Rev. B 5, 72 (1972).
- Kurilovich, V. D. & Glazman, L. I. Criticality in the crossed Andreev reflection of a quantum Hall edge, Phys. Rev. X 13, 031027 (2023).
- 34. Li. C. et al. Magnetic field resistant quantum interferences in Josephson junctions based on bismuth nanowires, Phys. Rev. B 90, 245427 (2014).
- Murani, A. et al. Ballistic edge states in Bismuth nanowires revealed by SQUID interferometry. Nat. Commun. 8, 15941 (2017).

Publisher's note Springer Nature remains neutral with regard to jurisdictional claims in published maps and institutional affiliations.

Springer Nature or its licensor (e.g. a society or other partner) holds exclusive rights to this article under a publishing agreement with the author(s) or other rightsholder(s); author self-archiving of the accepted manuscript version of this article is solely governed by the terms of such publishing agreement and applicable law.

© The Author(s), under exclusive licence to Springer Nature Limited 2024

Methods

Device fabrication

MTGBs were prepared using the 'cut and stack' method 36,37 with rotation by an angle of less than 0.1° . Such stacks of graphene monolayers are known to form relatively large domains of bilayer graphene with the Bernal stacking order (AB and BA), which are separated by narrow (approximately 10 nm) domain walls $^{14-16,26-28,38}$. After assembly during which the MTGBs were placed on top of hexagonal boron nitride (hBN) crystals, the domain structure could be visualized by piezo-force microscopy shown in Extended Data Fig. 1a. We made several Josephson junction devices using domain walls visualized by this technique. However, none of them exhibited proximity superconductivity in the quantum Hall regime. We attribute this to further structural changes such that the domain walls slipped away from the proximity regions after the fabrication of closely spaced superconducting contacts. The electronic quality of the resulting Josephson junctions was also poor.

To preserve the graphene quality, we made MTGB structures fully encapsulated in hBN. Unfortunately, piezo-force microscopy could not be used once an insulating hBN layer was placed on top of the MTGBs (ref. 39). To overcome this problem, we tried different methods to visualize the domain walls within encapsulated MTGBs and eventually used scanning photocurrent microscopy⁴⁰. This dedicated technique is described in detail in ref. 40. Briefly, it utilizes scanning near-field optical microscopy to focus an infrared laser onto a region of interest and measures the induced photovoltage between two nearby electrodes. The resulting signal provides micrographs, such as the one shown in Extended Data Fig. 1b,c in which the domain walls appear as blurred white stripes between red and blue regions representing neighbouring AB and BA domains⁴⁰. Note that other approaches based on scanning near-field optical microscopy have been used previously to visualize domain walls in twisted bilayers and have revealed the characteristic triangular pattern^{17,41,42}. However, for hBN-encapsulated MTGBs and in the absence of such a pattern at minimal twist angles, we found those approaches insufficient to distinguish isolated domain walls from other inhomogeneities.

Using the imaged domain structures, we designed Josephson junctions by trying to align domain walls along the shortest distance between the superconducting electrodes (Extended Data Fig. 1c), and we made devices with different numbers $N_{\rm DW}$ of domain walls. Electron-beam lithography and dry etching were then employed to embed the superconducting electrodes at the chosen positions (Extended Data Fig. 1c,d). For the superconductor, we used 60 nm of NbTi (atomic ratio of 55 to 45%) with a 3-nm-thick adhesion layer of Ta. An additional 3 nm of Ta followed by 5 nm of Pt were deposited on top of the NbTi to protect it from oxidation. The four-layer film was deposited by radio-frequency sputtering at a rate of 6 nm min⁻¹ under a controlled argon pressure of approximately 10⁻⁵ bar. The NbTi electrodes were found to exhibit $T_c \approx 7.0$ K and $H_{c2} \approx 9.5$ T. They were separated by a distance L = 100 to 200 nm and had a width W between 0.5 and 4 μm (Extended Data Fig. 1e). The devices were assembled and fabricated on top of an oxidized Si wafer, which also served as a back gate to vary the carrier concentration n in the MTGBs.

Characterization of MTGB junctions

Electrical measurements were carried out in a dilution refrigerator (Oxford Instruments Triton). The standard low-frequency lock-in technique (less than 150 Hz) was employed using a.c. currents $I_{\rm ac}$ within a few nanoamperes range. For measurements of nonlinear IV characteristics, $I_{\rm ac}$ was superimposed on top of d.c. currents $I_{\rm dc}$ ranging from nanoamperes to microamperes. Both the a.c. and d.c. currents were sourced directly from lock-in amplifiers (Zurich Instruments). With decreasing $I_{\rm ac}$, differential resistance curves, as shown in, for example, Fig. 1c and Extended Data Fig. 8b,d, stopped evolving below 2 nA (that is, they did not get sharper with decreasing $I_{\rm ac}$), which indicated the

level of electronic noise affecting our devices. The noise also limited the lowest electronic temperature (T) achievable for our devices to approximately 50 mK. Most measurements were done using $I_{\rm ac}$ between 2 and 5 nA, which represented a compromise between keeping $I_{\rm ac}$ as low as possible and avoiding noise on dV/dI curves, given the chosen (rather long) time constant of 1 s. Depending on the desired range for IV characteristics, $I_{\rm dc}$ was applied in small steps $\Delta I_{\rm dc}$, varying from less than 1 nA to approximately 50 nA.

We first characterized each of the studied Josephson junctions in the normal state by measuring its two-probe resistance R_{2p} as a function of B and n at temperatures above T_c , typically at 10 K. In the absence of a gate voltage, all our devices were found to be slightly doped, typically by approximately 5×10^{11} cm⁻². An example of the obtained maps $R_{2p}(n,B)$ is shown in Extended Data Fig. 2a for an MTGB junction with a single domain wall connecting NbTi electrodes. All the devices, independent of their design and $N_{\rm DW}$, exhibited pronounced SdH oscillations that followed the sequence of filling factors v = 0, 4, 8, 12, ..., as expected for Bernal-stacked bilayer graphene. Quantum Hall plateaus were neither expected 43 nor observed for this two-probe geometry.

By comparing junctions with different numbers of domain walls, we noticed a clear correlation between N_{DW} and R_{2D} at v = 0 (neutrality point), such that the magnetoresistance monotonically decreased with increasing $N_{\rm DW}$. The correlations are illustrated in Extended Data Fig. 2b, which plots the neutrality-point conductance $G_{v=0} = 1/R_{2n}(v=0)$ as a function of B for junctions with different N_{DW} . In fields above 6 T, all the two-probe curves exhibited slowly saturating B dependences. For junctions without domain walls ($N_{DW} = 0$), $G_{v=0}$ saturated to small values that varied from junction to junction but were always less than $4e^2/h$ (note that $W/L \gg 1$, so that the graphene resistivity was more than $100 \,\mathrm{k}\Omega$ per square at liquid helium T), in agreement with the presence of a small gap at v = 0, which is expected because of both finite doping and exchange interactions⁴⁴. Furthermore, Extended Data Fig. 2c compares devices with and without domain walls at a fixed B = 14 T over a wider range of T. The latter device $(N_{DW} = 0)$ exhibited a thermally activated behaviour at the neutrality point, consistent again with a small gap being present. In stark contrast, for the device with a single domain wall, $R_{2n}(v=0)$ remained practically constant over the entire T range (Extended Data Fig. 2c), suggesting that the domain wall provided an additional conducting channel.

To quantify the conductance of the domain wall channel, we employed two complementary approaches. Using curves such as Extended Data Fig. 2b, we calculated the excess conductance, $\delta = G_{v=0}(N_{\rm DW}) - G_{v=0}(N_{\rm DW} = 0)$, for Josephson junctions with domain walls. The particular junction with one domain wall in Extended Data Fig. 2b exhibited $\delta \approx 0.8 \times 4e^2/h$ at 10 T. The junction with two domain walls had an excess conductance that was twice (within 10%) that of the one-domain wall junction for all B > 6 T. Alternatively, assuming that the contact resistance between the domain walls and superconducting electrodes was close to the R_{2p} value reached in the limit of high electron doping in which the $R_{2n}(n)$ curves are saturated (Extended Data Fig. 2c), we subtracted this value as a contact resistance from $R_{2p}(v=0)$ to obtain the domain wall resistance itself. The corresponding $G_{\nu=0}$ is plotted in Extended Data Fig. 2d, which again shows that a single domain wall provided a conductance of approximately $4e^2/h$. This value is also consistent with the known electronic structure of AB/BA domain walls. Indeed, in the presence of a gap at the neutrality point, the domain walls are known to support counterpropagating (chiral) edge states, which each contribute the conductance quantum e^2/h . The factor of 4 comes from the spin and valley degeneracy^{16,26}. Based on these observations, we used the saturation value of $G_{v=0}$ to estimate $N_{\rm DW}$ for the studied MTGB junctions and compared it with the number of domain walls seen using photocurrent scanning microscopy. Good agreement between the two values was found. The estimate for $N_{\rm DW}$ using the conductance of the Josephson junctions at v = 0 was particularly useful for the devices with many domain walls, as it was difficult to resolve individual walls by photocurrent microscopy. Further support for the estimates described was found by comparing the critical currents I_c in junctions with different $N_{\rm DW}$ (next section and Extended Data Fig. 3c,d).

Supercurrents in junctions with several domain walls

To illustrate how the critical current evolved with the number of domain walls, Extended Data Fig. 3a,b shows plots for large $N_{\rm Dw}\approx 15$. The plots are provided in the same representation as Fig. 1b,c for a single domain wall. At zero field, low T and for strong electron doping $n>10^{12}$ cm⁻², the critical current I_c was of the order of a few microamperes per micrometre width of the Josephson junction. This zero-B value did not show any systematic dependence on $N_{\rm Dw}$. At low B, all our Josephson junctions also exhibited pronounced deviations from the standard Fraunhofer pattern^{20,25}, independently of $N_{\rm Dw}$ (compare Extended Data Fig. 3a for $N_{\rm Dw}\approx 15$, Fig. 1b for $N_{\rm Dw}=1$ and Fig. 3a of ref. 20 for $N_{\rm Dw}=0$). Such deviations are characteristic of ballistic Josephson junctions and discussed in detail in ref. 20. In general, the observed behaviour shows that the presence of AB/BA domain walls has little effect on proximity superconductivity at low B.

In the quantum Hall regime, for which the cyclotron diameter $2r_c$ is smaller than the junction length L so that no ballistic transport can occur through the graphene bulk object of and wider zero-resistance states than those junctions with small $N_{\rm DW}$ (compare Fig. 1c and Extended Data Fig. 3b). Importantly, no supercurrent could be observed in the quantum Hall regime for any Josephson junctions without domain walls (Extended Data Fig. 5). These observations are quantified in Extended Data Fig. 3c in which I_c is seen to increase roughly proportional to $N_{\rm DW}$. This dependence suggests that each domain wall provided an independent Andreev channel capable of carrying a certain amount of supercurrent. Away from H_{c2} , the supercurrent was approximately 10 nA per domain wall at low T, as shown in Extended Data Fig. 3d.

To complete the comparison between Josephson junctions with different numbers of domain walls, Extended Data Fig. 4 shows differential resistance maps $dV/dI(B, I_{dc})$ over a very wide range of B for junctions containing a few and many domain walls. These plots should be compared with the single domain wall in Fig. 1d. Qualitatively, all the plots look rather similar. The supercurrent in the Josephson junctions survived in the quantum Hall regime up to fields comparable to H_{c2} in the NbTi contacts, and $I_c(B)$ exhibited pronounced rapid fluctuations. independently of the number of domain walls involved, if at least one domain wall was present (see the next section). Nonetheless, there are a couple of notable differences. First, in Josephson junctions with many domain walls, finite critical currents persisted into consistently higher B. This is particularly obvious in Extended Data Fig. 4b where finite I_c can be observed in fields reaching above 8 T, that is, less than 20% from H_{c2} (compare this figure with Fig. 1c,d and Extended Data Fig. 4a). The increased *B* range of proximity superconductivity for Josephson junctions with large $N_{\rm DW}$ can be attributed to the simple fact that the external noise and finite I_{ac} smeared our dV/dI curves, so that we could detect induced superconductivity only if $I_c(B)$ exceeded a few nanoamperes. Accordingly, if many domain walls contributed to the critical current, our detection threshold was breached at somewhat higher B. Second, in contrast to a single domain wall, Josephson junctions with many domain walls did not exhibit a clear transition from fluctuating to non-fluctuating $I_c(B)$ after entering the quantum Hall regime (compare Extended Data Fig. 4b with Fig. 1d). The strongly fluctuating $I_c(B)$ in the quantum Hall regime for large $N_{\rm DW}$ can be attributed to quantum interference between supercurrents carried by different domain walls in parallel. Such interference oscillations are nearly random because many different areas are involved. The randomness is also expected to suppress the absolute value of the maximum I_c by a factor of 3–5 with respect to one or two domain walls. More importantly, vortices entering superconducting contacts in the vicinity of domain walls suppress the proximity, as seen on our experimental curves. This effect is much more pronounced in the multidomain devices (see, for example, Fig. 1 and Extended Data Fig. 4), as discussed in the section 'Steady supercurrent along a single domain wall'.

losephson junctions without domain walls

To demonstrate that the robust supercurrents observed in the quantum Hall regime were due to domain walls rather than any other possible mechanism^{1,2,6,20,22,23,45-47}, we studied Josephson junctions without domain walls between superconducting electrodes (Extended Data Fig. 5). Otherwise, they were made using the same design and fabrication procedures as described above. The first type of these reference devices was based on AB-stacked bilayer graphene. These Josephson junctions were made either directly from exfoliated bilaver graphene or utilized regions of MTGB stacks with no domain walls (Extended Data Fig. 5a). The other reference devices incorporated either wrinkles that commonly occurred during stacking of van der Waals heterostructures (Extended Data Fig. 5b) or nanoscale slits made by high-resolution electron-beam lithography (Extended Data Fig. 5c). The general idea is that such defects in graphene can support closely spaced counterpropagating quantum Hall edge states^{1,2,6,20,22,23,45-47}. In intermediate magnetic fields $(2r_c > L)$, all three types of Josephson junction exhibited similar behaviour with large fluctuations in $I_c(B)$ and interspersed pockets of the zero-resistance state (Extended Data Fig. 5). This behaviour is like that of our Josephson junctions with domain walls and, again, is attributed to ballistic transport of Andreev bound states between the superconducting electrodes^{20,25}. Note that the device in Extended Data Fig. 5b was edgeless, which explains the suppression of proximity superconductivity at much lower B compared with our edged Josephson junctions, including those shown in Extended Data Fig. 5a,c. Indeed, fluctuations in $I_c(B)$ rely on electron trajectories scattered by sample edges or extended defects²⁰ and are expected to be severely suppressed in edgeless Josephson junctions with parallel superconducting electrodes, in agreement with the experiment.

Importantly, none of our many reference devices exhibited any sign of proximity superconductivity in the quantum Hall regime $(2r_c < L)$. Let us emphasize that no critical current in quantizing B could be detected even for Josephson junctions with the narrowest slits that were less than 10 nm wide (Extended Data Fig. 5c). In this case, one can imagine Andreev states formed by quantum Hall edge states that counterpropagate along the slit edges and are proximity-coupled through the superconducting electrodes²³. In our slit devices, the gap in graphene was close to the coherence length of NbTi, $\xi \approx 6$ nm, but still no supercurrent could be discerned at high B. This observation agrees with recent attempts to implement the same idea using counterpropagating quantum Hall states, either in different graphene layers²⁴ or across somewhat wider slits (approximately 30 nm)²³. All the evidence-from our experiments and the literature-indicates that AB/BA domain walls are unique in their ability to support Andreev bound states in quantizing B.

Steady supercurrent along a single domain wall

In the quantum Hall regime, Josephson junctions with several domain walls exhibited pronounced fluctuations in $I_c(B)$ with a characteristic period of the order of one flux quantum ϕ_0 piercing the junction area $W \times L$. Accordingly, these oscillations were attributed to quantum interference loops made of supercurrents propagating along different paths^{2,6,22}. No oscillations with either such a short periodicity or a much longer one could be observed for junctions containing a single domain wall (Fig. 2). The absence of quantum interference oscillations in Josephson junctions with a single domain wall is reiterated by Extended Data Fig. 6. The figure shows that, like the device in Fig. 2b, the critical current in the quantum Hall regime was constant over rather large field intervals (Extended Data Fig. 6b,c). The junction in Extended Data Fig. 6 exhibited a monotonic decay of I_c with increasing B, which is somewhat

different from the steadier behaviour for the single-domain-wall device described in the main text (Fig. 1d). Nonetheless, the characteristic field interval ΔB over which the critical current changed considerably was at least a few tesla (Extended Data Fig. 6a). This again shows that any possible quantum loop made of either two supercurrent paths or counterpropagating electrons and holes forming an Andreev bound state could not be wider than $d \approx \phi_0/\Delta BL$, approximately a few nanometres, which is less than ξ .

The abrupt changes in the critical current with varying *B*, which are seen clearly in Fig. 1d, were attributed to superconducting vortices suddenly changing their positions in the vicinity of the one-dimensional–three-dimensional contacts between domain walls and superconducting electrodes. To corroborate this explanation, Extended Data Fig. 7 shows two maps that were measured for the same Josephson junction containing a single domain wall when sweeping the magnetic field up and down. The random nature of the jumps suggests that there had been rearrangements of vortices that were pinned within the superconducting contacts.

Temperature dependence of the critical current

It is instructive to compare the temperature dependences of $I_{\rm c}$ in low and quantizing fields (Extended Data Fig. 8). At low B, in which the proximity superconductivity is dominated by two-dimensional Andreev-bound-state transport through the bilayer graphene bulk, we observed behaviour like that reported previously for ballistic Josephson junctions made from monolayer graphene 20,31 . At T > 2 K, the critical current is described well by the exponential dependence 31,32 :

$$I_{\rm c}(T) \propto \exp(-k_{\rm B}T/\delta E),$$
 (1)

where $k_{\rm B}$ is the Boltzmann constant. This dependence is characteristic of so-called long Josephson junctions, in which the suppression of $I_{\rm C}$ is caused by thermally induced decoherence between energy levels of quantum-confined Andreev bound states. In ballistic junctions, δE is expected to be approximately $hv_{\rm F}/4\pi^2L$ (refs. 31,32), which we estimate as approximately 0.3 meV for the device in Extended Data Fig. 8, taking into account the density-dependent Fermi velocity $v_{\rm F}$ in bilayer graphene but ignoring the penetration of Andreev bound states into the superconducting electrodes 32 . The latter effectively increases L and makes δE smaller. The fit in Extended Data Fig. 8a yields $\delta E \approx 0.2$ meV (white dashed curve), in good agreement with the theoretical estimate. This conclusion about the long-junction regime and the absolute value of δE agrees with a previous analysis for ballistic Josephson junctions made from monolayer graphene 20,31 .

At T < 2 K, zero-B differential resistance curves became hysteretic, exhibiting different superconducting boundaries when sweeping the d.c. current up and down. This is seen in Extended Data Fig. 8a,b as a notable asymmetry for positive and negative $I_{\rm dc}$. The transition between zero- and finite-resistance states happened abruptly, which resulted in dV/dI seemingly diverging at the transition (Extended Data Fig. 8b). The hysteretic behaviour is typical of underdamped Josephson junctions in which the switching current no longer represents the true $I_{\rm c}$ (ref. 48).

In quantizing B, the measured dV/dI curves were non-hysteretic and fully symmetric at all T. This is shown in Extended Data Fig. 8c,d for B=3 T, which is well above the onset of the quantum Hall regime but sufficiently below $H_{\rm c2}$. Superficially, the temperature dependence in Extended Data Fig. 8c looks different from that in Extended Data Fig. 8a. Accordingly, it is tempting to attribute this change to a transition into the short-junction regime at high B, where $I_{\rm c}(T)$ would no longer decrease exponentially with increasing T but is expected to vary more gradually (roughly as the superconducting gap) 31,49 . The regime change also seems plausible because of the transition from two-dimensional transport through the graphene bulk to one-dimensional transport along domain walls. However, note that $I_{\rm c}$ in the quantum Hall regime

at high T was comparable to the probing current $I_{\rm ac}$ (Extended Data Fig. 8c,d). Accordingly, there could be a tail of small $I_{\rm c}$ extending to higher T, as in Extended Data Fig. 8a. Such a tail would be smeared by small but finite $I_{\rm ac}$ and background radiation. Because of the smearing, the behaviour in Extended Data Fig. 8c is inconclusive but, nonetheless, consistent with the long-junction regime, especially as the supercurrent in the quantum Hall regime (Extended Data Fig. 8c) disappeared at $T \ll T_{\rm c}$ and was much smaller than in zero B (Extended Data Fig. 8a).

Shapiro steps for one-dimensional Josephson junctions

For completeness, we show that the proximity superconductivity along domain walls in MTGBs could also be observed as the inverse a.c. Josephson effect. The latter effect arises from phase locking between microwave (radio-frequency) radiation and the supercurrent through Josephson junctions, which leads to so-called Shapiro steps in IV characteristics. The steps appear at quantized voltages:

$$V_{\rm M} = M\phi_0 f_{\rm rf}, \tag{2}$$

where $f_{\rm rf}$ is the radiation frequency and M the step index^{50,51}. In our experiments, the radio-frequency excitation was provided by a signal generator (R&S SMB100A) and transmitted through semi-rigid coaxial cables thermally anchored to different stages of the dilution refrigerator, with attenuation of approximately 35 dB. The devices were irradiated from the cable's open end, which was approximately 1 mm away from the Josephson junctions studied.

The Shapiro steps observed in the quantum Hall regime for Joseph-son junctions with one or several domain walls are shown in Extended Data Fig. 9. Extended Data Fig. 9a illustrates how the IV characteristics evolved as a function of the radio-frequency power P at a fixed frequency. The steps gradually appeared and disappeared on varying the power, and higher-order steps are clearly visible. The separation ΔV between steps increased linearly with the radiation frequency and is accurately described by equation (2) (inset of Extended Data Fig. 9a). The width $\Delta I_{\rm M}$ of the Shapiro steps is expected to follow the equation 51 :

$$\Delta I_{\rm M} = |\mathcal{J}_{\rm M}(V_{\rm rf}/\Delta V)|,\tag{3}$$

where \mathcal{J}_{M} is the Bessel function of order M, and V_{rf} is the a.c. (radiation) voltage applied to the junction. To determine ΔI_{M} experimentally, we measured the differential resistance $\mathrm{d}V/\mathrm{d}I(I_{\mathrm{dc}})$ as a function of the radio-frequency power for fixed B, n and f_{rf} (Extended Data Fig. 9b–d). Because $V_{rf} = \alpha P^{1/2}$, we used the proportionality coefficient α as a single fitting parameter to scale the x axes for these plots and obtain the best agreement with equation (3)⁵¹. The pink curves in Extended Data Fig. 9b–d show examples of the expected boundary positions for the Shapiro steps. A detailed analysis of ΔI_{M} for the first four steps is provided in Extended Data Fig. 9e. Good agreement between the experiment and equation (3) is found for all our Josephson junctions measured under radio-frequency radiation and for both maxima and minima of the supercurrent flowing along domain walls (Extended Data Fig. 9b,c).

Fabry-Pérot oscillations in the critical current in the quantum Hall regime

As discussed in the main text, our Josephson junctions with AB/BA domain walls exhibited pronounced Fabry–Pérot oscillations at the critical current. These appeared only in the quantum Hall regime as the MTGB conductance was dominated by electron transport along domain walls. An example of these oscillations is shown in Fig. 3b. Further details of the oscillatory behaviour are provided in Extended Data Fig. 10, which compares differential resistance maps dV/dI(n,B) at zero and high d.c. biases. In the latter case ($I_{\rm dc}=100$ nA) and for fields above 1 T, the Josephson junctions were pushed into the normal state, in which SdH oscillations appeared (Section 'Characterization of MTGB

junctions' above; and Extended Data Fig. 10a). For zero bias ($I_{dc} = 0$), the resistance maps exhibited strong additional oscillations (Extended Data Fig. 10b). These clearly emerged after the entry into the quantum Hall regime $(2r_c < L)$ and, for the Josephson junction in Extended Data Fig. 10, persisted up to 6 T. The oscillations exhibited small changes in their *n* positions with increasing *B*, which occurred in the direction opposite to that of SdH oscillations (Extended Data Fig. 10b). This unequivocally shows that the former oscillations were not related to Landau quantization. Note that the Fabry-Pérot oscillations shown in Extended Data Fig. 10b do not represent oscillations in the critical current. Instead, the minima and maxima of dV/dI(n,B) reflect the contrasting steepness of IV characteristics at different positions on the map. Nonetheless, the observed maxima in the resistance maps are expected to indicate conditions under which electron transmission through Josephson junctions was minimal and, therefore, should also correspond to minima in I_c . To corroborate this consideration, we measured full $dV/dI(I_{dc})$ characteristics for many fields and carrier densities, extracted the critical current values directly and plotted them as a function of both n and B. This approach was extremely time-consuming, so that we had to resort to relatively large B steps of 0.5 T (Extended Data Fig. 10c). Nonetheless, Fabry-Pérot oscillations in the critical current are clearly seen on the latter map, and minima in I_c closely match maxima in the resistance oscillations of Extended Data Fig. 10b, as expected.

Minima in the critical current for Fabry-Pérot oscillations are expected to occur at integer $N = L/(\lambda_F/2)$ where λ_F is the Fermi wavelength. Under these conditions, interference between incident and reflected electron waves within the graphene cavity between superconducting contacts leads to standing waves^{20,25}. As seen in Fig. 3b and Extended Data Fig. 10b,c, the observed minima and maxima in I_c occurred approximately equidistantly along the n axis, despite n changing by more than an order of magnitude. This suggests that $\lambda_{\rm F}$ for the electrons responsible for the observed Fabry-Pérot resonances changed relatively little with n. Such behaviour cannot be explained assuming a two-dimensional electronic spectrum, as for the low-B Fabry-Pérot oscillations reported previously^{20,25}. Indeed, for any two-dimensional spectrum, $\lambda_F \propto n^{-1/2}$, which should lead to a square root dependence N(n) rather than the roughly linear one observed experimentally (Fig. 3c). To explain this surprising result, we calculated the electronic spectrum for one-dimensional electrons confined within AB/BA domain walls and found that λ_E is a function of gate doping (Supplementary Information). The resulting curve is plotted in Fig. 3c and shows good agreement between experiment and theory. In both cases, the dependences are slightly sublinear and, importantly, do not extrapolate to zero N in the limit of low densities. The latter observation reflects that AB/BA domain walls support a finite electron density within charge-neutral MTGBs (ref. 29). The observed small shift of the Fabry-Pérot resonances towards lower *n* with increasing *B* remains to be understood (Extended Data Fig. 10b,c). Tentatively, we attribute the shift to field-induced changes in an electrostatic confinement of one-dimensional electrons, which are not accounted for in the model described in ref. 29.

Data availability

The original data files that support the findings of this study are available at https://doi.org/10.5281/zenodo.10698874 (ref. 52) and from J.B.

- Saito, Y., Ge, J., Watanabe, K., Taniguchi, T. & Young, A. F. Independent superconductors and correlated insulators in twisted bilayer graphene. Nat. Phys. 16, 926–930 (2020).
- Stepanov, P. et al. Untying the insulating and superconducting orders in magic-angle graphene. Nature 583, 375–378 (2020).
- Lane, T. L. M. et al. Ballistic electron channels including weakly protected topological states in delaminated bilayer graphene. Phys. Rev. B 97, 045301 (2018).
- McGilly, L. J. et al. Visualization of moiré superlattices. Nat. Nanotechnol. 15, 580–584 (2020).
- Hesp, N. C. H. et al. Nano-imaging photoresponse in a moiré unit cell of minimally twisted bilayer graphene. Nat. Commun. 12, 1640 (2021).
- 41. Luo, Y. et al. In situ nanoscale imaging of moiré superlattices in twisted van der Waals heterostructures. *Nat. Commun.* 11, 4209 (2020).
- Sunku, S. S. et al. Photonic crystals for nano-light in moiré graphene superlattices. Science 362, 1153–1156 (2018).
- 43. Williams, J. R., Abanin, D. A., DiCarlo, L., Levitov, L. S. & Marcus, C. M. Quantum Hall conductance of two-terminal graphene devices. *Phys. Rev. B* **80**, 045408 (2009).
- Feldman, B. E., Martin, J. & Yacoby, A. Broken-symmetry states and divergent resistance in suspended bilayer graphene. *Nat. Phys.* 5, 889–893 (2009).
- Khaymovich, I. M., Chtchelkatchev, N. M., Shereshevskii, I. A. & Mel'nikov, A. S. Andreev transport in two-dimensional normal-superconducting systems in strong magnetic fields. *Europhys. Lett.* 91, 17005 (2010).
- Ma, M. & Zyuzin, A. Y. Josephson effect in the quantum Hall regime. Europhys. Lett. 21, 941 (1993).
- Gamayun, O., Hutasoit, J. A. & Cheianov, V. V. Two-terminal transport along a proximityinduced superconducting quantum Hall edge. *Phys. Rev. B* 96, 241104 (2017).
- 48. Tinkham, M. Introduction to Superconductivity 2nd edn (McGraw-Hill Book Co, 1996).
- 49. Golubov, A. A., Kupriyanov, M. Y. & Il'Ichev, E. The current-phase relation in Josephson junctions. *Rev. Mod. Phys.* **76**, 411 (2004).
- Shapiro, S. Josephson currents in superconducting tunneling: the effect of microwaves and other observations. *Phys. Rev. Lett.* 11, 80 (1963).
- Russer, P. Influence of microwave radiation on current-voltage characteristic of superconducting weak links. J. Appl. Phys. 43, 2008–2010 (1972).
- Barrier, J. Replication data for: One-dimensional proximity superconductivity in the quantum Hall regime. Zenodo https://doi.org/10.5281/zenodo.10698874 (2024).

Acknowledgements We acknowledge financial support from the European Research Council (Grant VANDER), the Lloyd's Register Foundation, Horizon 2020 Graphene Flagship Core3 Project and the Engineering and Physical Sciences Research Council (EPSRC; Grant Nos EP/V007033/1 and EP/S030719/1). J.B. acknowledges support from the EPSRC (Doctoral Prize fellowship). R.K.K. acknowledges the EU Horizon programme (Grants 754510, 893030) and the FLAG-ERA programme (PhotoTBG). L.I.G. was supported by the National Science Foundation (Grant DMR-2002275) and the Office of Naval Research (Award N00014-22-1-2764).

Author contributions A.K.G. and J.B. initiated and led the project. N.X. and P.K. fabricated the devices with help from L.H. Domain walls in MTGBs were imaged by R.K.K., F.H.L.K. and R.V.G. J.B. carried out the electrical measurements with help from M.K., E.N., A.I.B. and J.R.P. J.B. and A.K.G. analysed the data with help from I.V.G., L.I.G., J.R.P. and V.I.F. C.M., V.V.E., L.I.G. and V.I.F. provided theoretical support. K.W. and T.T. supplied quality hBN crystals. J.B., I.V.G. and A.K.G. wrote the manuscript with contributions from N.X. and V.I.F. All authors contributed to discussions.

Competing interests The authors declare no competing interests.

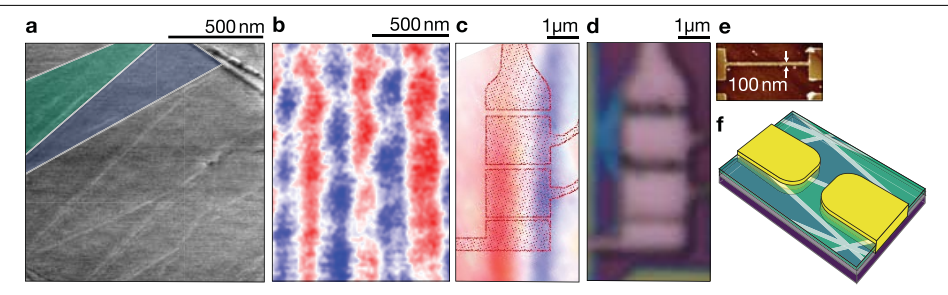
Additional information

Supplementary information The online version contains supplementary material available at https://doi.org/10.1038/s41586-024-07271-w.

Correspondence and requests for materials should be addressed to Julien Barrier, Na Xin or A. K. Geim.

Peer review information *Nature* thanks Ivan Borzenets and the other, anonymous, reviewer(s) for their contribution to the peer review of this work.

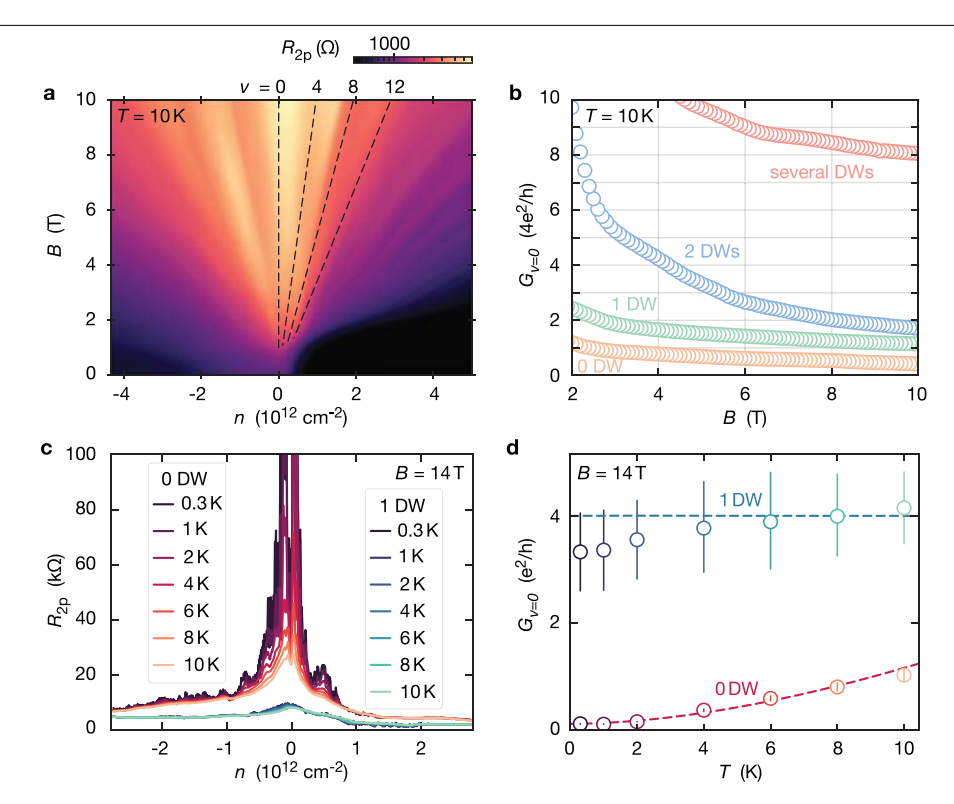
Reprints and permissions information is available at http://www.nature.com/reprints.



Extended Data Fig. 1|Josephson junctions with AB/BA domain walls.

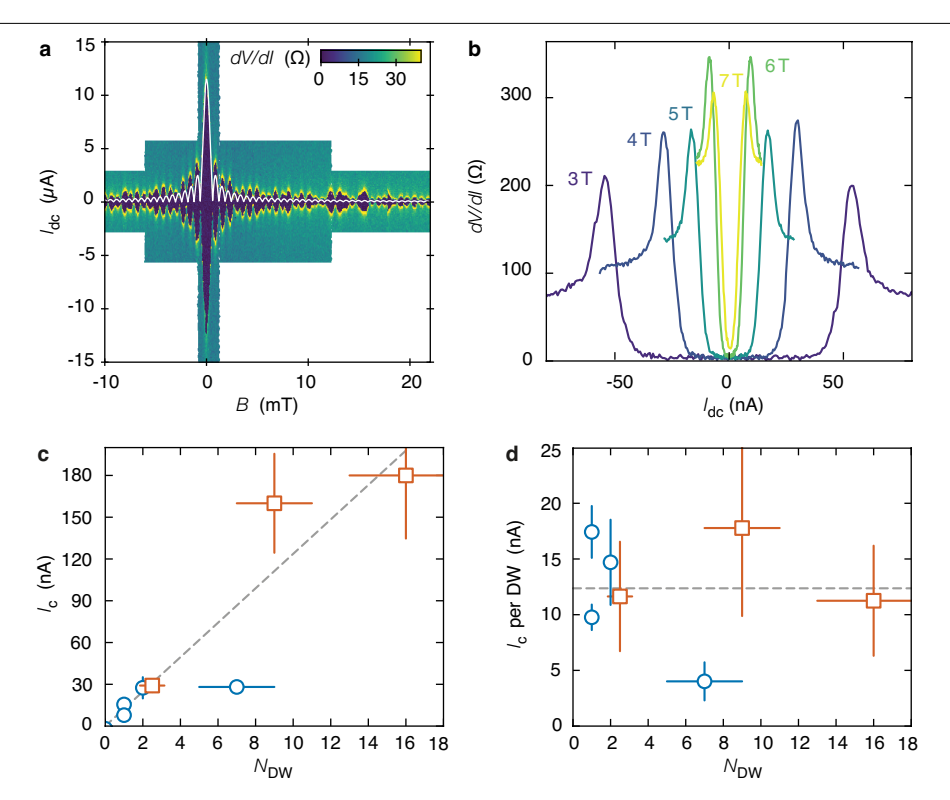
(a) Piezo-force micrograph showing domains in an MTGB before its encapsulation in hBN. The blue and green triangles indicate two neighboring regions with AB and BA stacking. (b) Photocurrent map for one of our fully encapsulated MTGB stacks that was used to make the studied Josephson junctions (photoexcitation energy of 188 meV, $n \approx 10^{12} \, \mathrm{cm}^{-2}$). Negative photocurrents are shown in blue, positive in red, and the white stripes in between reveal domain walls 40 . (c) Photocurrent map of a chosen domain walls with an overlaid design for superconducting electrodes, which is shown by

the shaded red areas. (d) Optical micrograph of the same region as in panel c after depositing the electrodes. (e) Atomic-force microscopy (AFM) image of one of the studied Josephson junctions. The darker areas correspond to superconducting electrodes. (f) Schematic of our 'edgeless' devices where MTGBs extended beyond the width $\mathcal W$ of Josephson junctions to avoid the presence of graphene edges in between the electrodes (compare with our 'edged' devices in Fig. 1a of the main text). The greenish triangles represent different AB and BA domains.



Extended Data Fig. 2 | **Normal-state transport. (a)** Typical Landau fan diagram for our MTGB devices. This particular junction contained a single domain wall and had $L \approx 150$ nm. The filling factors v indicated by the dashed lines were calculated using the known capacitance to the back gate; T = 10 K. (b) Two-probe conductance at the neutrality point as a function of B for different N_{DW} . For all

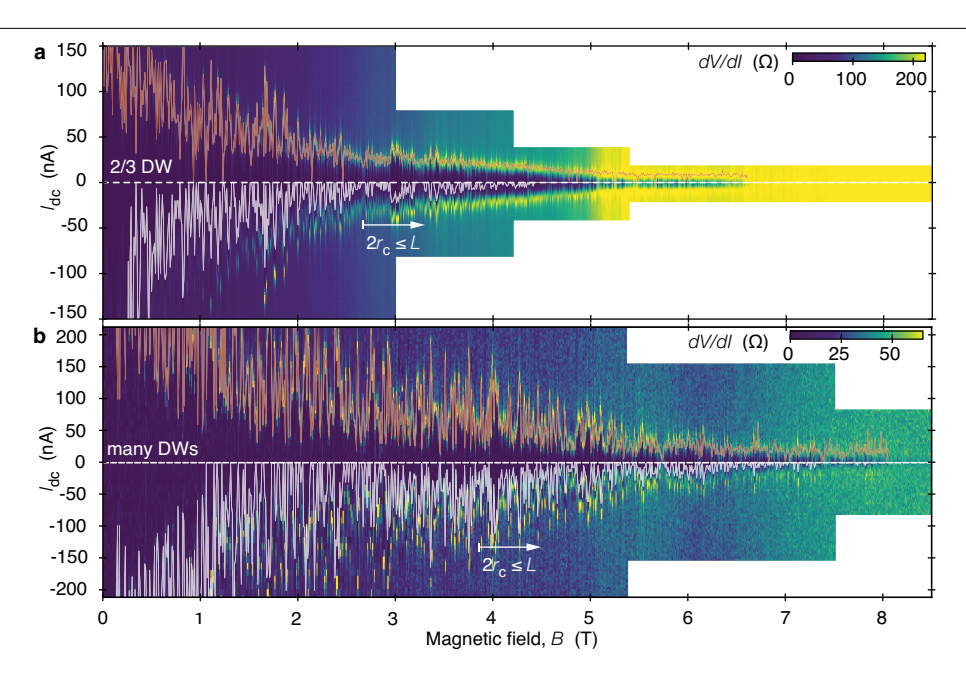
the plotted junctions, L was between 150 and 200 nm; T=10 K. (c) Resistance as a function of gate-induced n at different T for two representative junctions with 0 and 1 domain walls at 14 T ($L\approx200$ and 150 nm, respectively). Both junctions were 'edged'. (d) Corresponding conductance at v=0 (after subtracting relatively small contact resistances).



Extended Data Fig. 3 | Supercurrent carried by AB/BA domain walls.

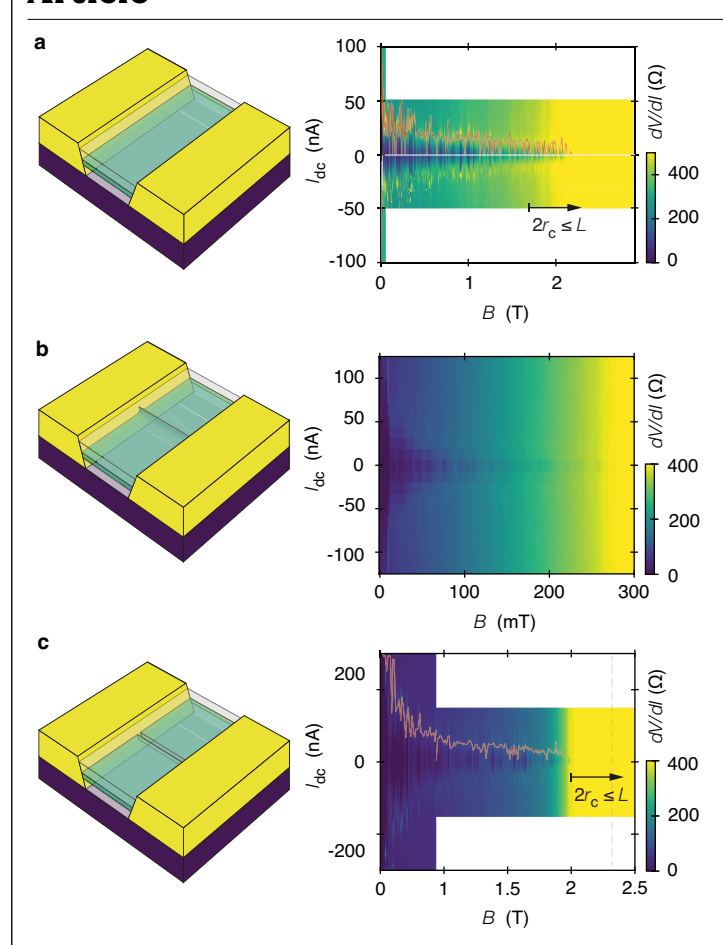
(a) Fraunhofer pattern typical for MTGB junctions. The shown Josephson junction was edgeless and contained 15 ± 3 domain walls. Measurements were done using steps in B of $60\,\mu\text{T}$. White curve: standard Fraunhofer dependence $I_c(B)$ calculated using the critical current at zero B and the apparent period for the first few oscillations. The deviations from the standard behavior are caused by ballistic transport of electrons and holes forming Andreev bound states 20,25 . (b) Differential resistance of the same junction in quantizing fields. For both (a)

and (b): $T \approx 50$ mK, $n \approx 2 \times 10^{12}$ cm $^{-2}$, $I_{\rm ac} = 5$ nA. (c) Critical current for different $N_{\rm DW}$ (B = 3 T, electron doping of $\approx 3 \times 10^{12}$ cm $^{-2}$, $T \approx 50$ mK in all cases). Blue symbols, edged junctions; orange, edgeless ones. The dashed line is the best linear fit. The horizontal error bars are caused by uncertainty in estimating the number of domain walls within the Josephson junctions. The vertical bars appear because I_c rapidly fluctuated with changing B and oscillated with n (Extended Data Figs. 4, 7; Fig. 3b of the main text) so that we plotted its rms values. (d) Same as in panel c but normalized by the number of domain walls.

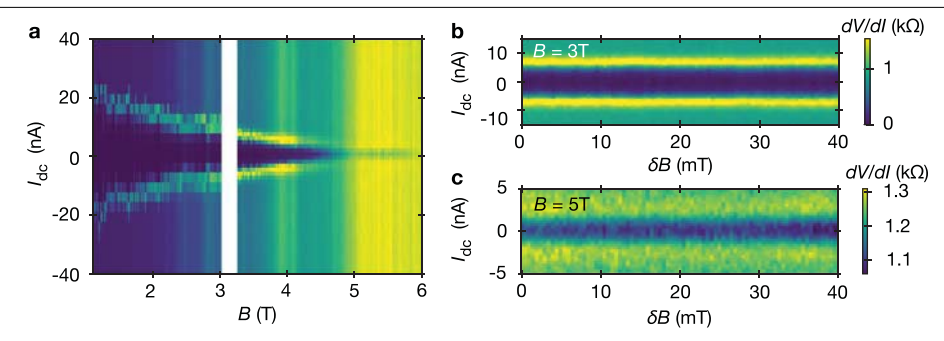


Extended Data Fig. 4 | Superconductivity in Josephson junctions with multiple domain walls. (a and b) Differential resistance for junctions with a few (estimated as 2 or 3) and many (16 \pm 3) domain walls, respectively. $I_{\rm ac}$ = 5 and 2 nA; $n\approx$ 2 and 3×10^{12} cm $^{-2}$, respectively. $T\approx$ 50 mK. Both junctions were

edgeless. The white curves in the bottom halves mark the boundaries of the zero-resistance state. The red curves in the top halves, the critical current. The step size in B was 10 mT.

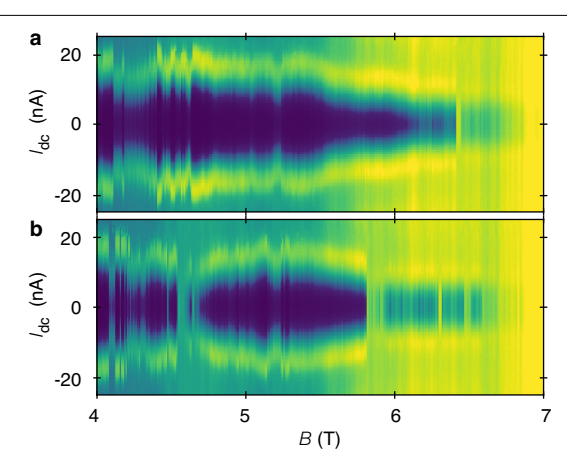


Extended Data Fig. 5 | **No supercurrent in the quantum Hall regime in reference devices.** Left column, schematics of Josephson junctions. Right column, corresponding differential resistance maps at high electron doping $n \approx 3 \times 10^{12} \text{cm}^{-2}$ and $L \approx 200$ nm for all the panels. Red curves, critical current. (a) Junction made from Bernal bilayer graphene. $W \approx 1 \, \mu \text{m}$, $I_{ac} = 5 \, \text{nA}$, $T \approx 50 \, \text{mK}$, $\Delta I_{dc} = 1 \, \text{nA}$. (b) Junction with a wrinkle formed in monolayer graphene. The wrinkle's full width was $\leq 100 \, \text{nm}$ as measured by AFM. $W \approx 1 \, \mu \text{m}$, $I_{ac} = 7 \, \text{nA}$, $T \approx 50 \, \text{mK}$, $\Delta I_{dc} = 15 \, \text{nA}$. (c) Monolayer graphene with a very narrow slit. Its width estimated by AFM was $< 10 \, \text{nm}$. $W \approx 4 \, \mu \text{m}$, $I_{ac} = 5 \, \text{nA}$, $T \approx 1 \, \text{K}$, $\Delta I_{dc} = 1 \, \text{nA}$. The junction in panel **b** was edgeless; panels **a** and **c** show edged Josephson junctions.

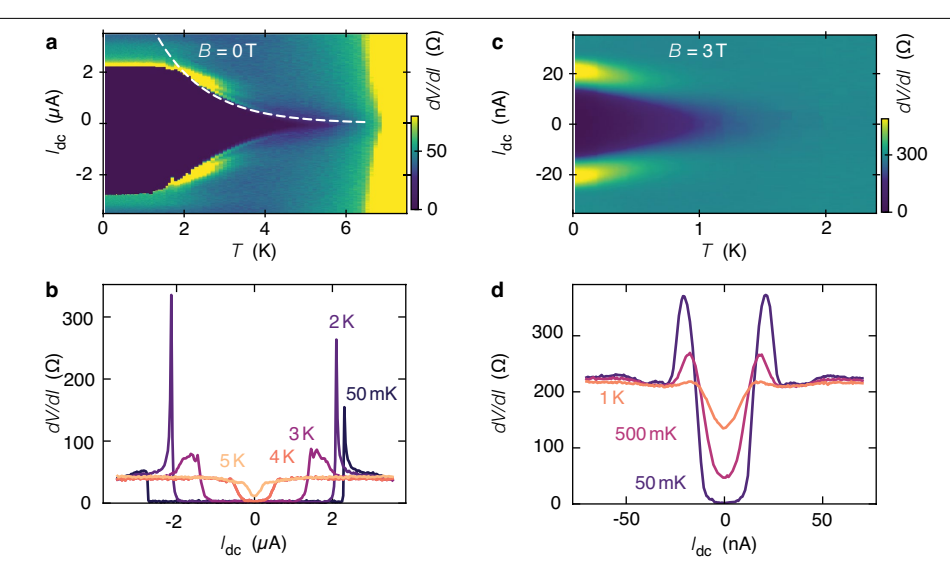


Extended Data Fig. 6 | Differential resistance maps for another junction with a single domain wall. (a) Map over a large interval of B (composed of two parts where the white gap indicates no data taken). Shown is an edged junction with $L \approx 150$ nm and $W \approx 0.5$ µm. Red curve, critical current. The digital noise is caused by finite steps in current: $\Delta I_{dc} = 3.3$ and 1.3 nA below and above 3 T,

respectively. Step size in B, 5 mT. ($\bf b$ and $\bf c$) Detailed maps around 3 and 5 T, respectively. Step size in B, 0.5 mT. $\Delta I_{\rm dc}$ = 0.6 and 0.3 nA for panels $\bf b$ and $\bf c$, respectively. For all the panels, $T\approx 50$ mK, $n\approx 1.7\times 10^{12}$ cm⁻², $I_{\rm ac}=2$ nA. Same color scales for panels $\bf a$ and $\bf b$.

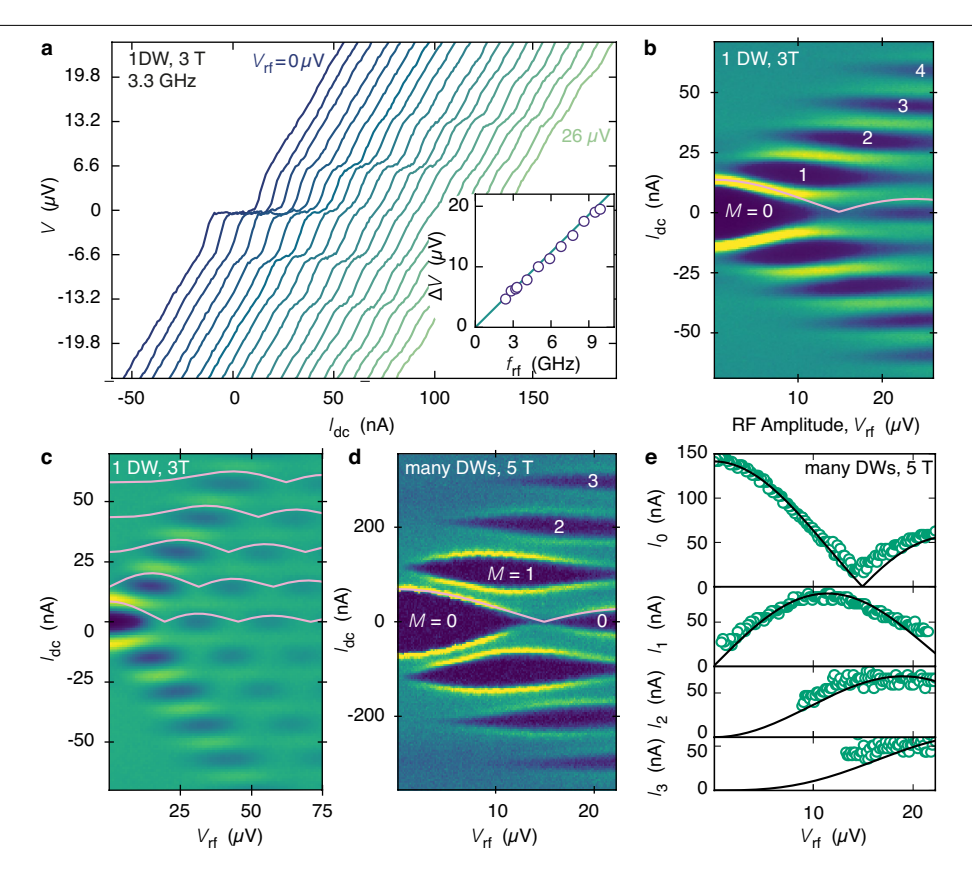


Extended Data Fig. 7 | **Vortices affect the critical current in the quantum Hall regime.** Differential resistance maps for increasing (**a**) and decreasing (**b**) magnetic field in steps of 10 mT. Same device as in Fig. 1 of the main text. $T \approx 50$ mK, $n \approx 2.1 \times 10^{12}$ cm⁻², $I_{ac} = 5$ nA. Same color scale as in Fig. 1d of the main text



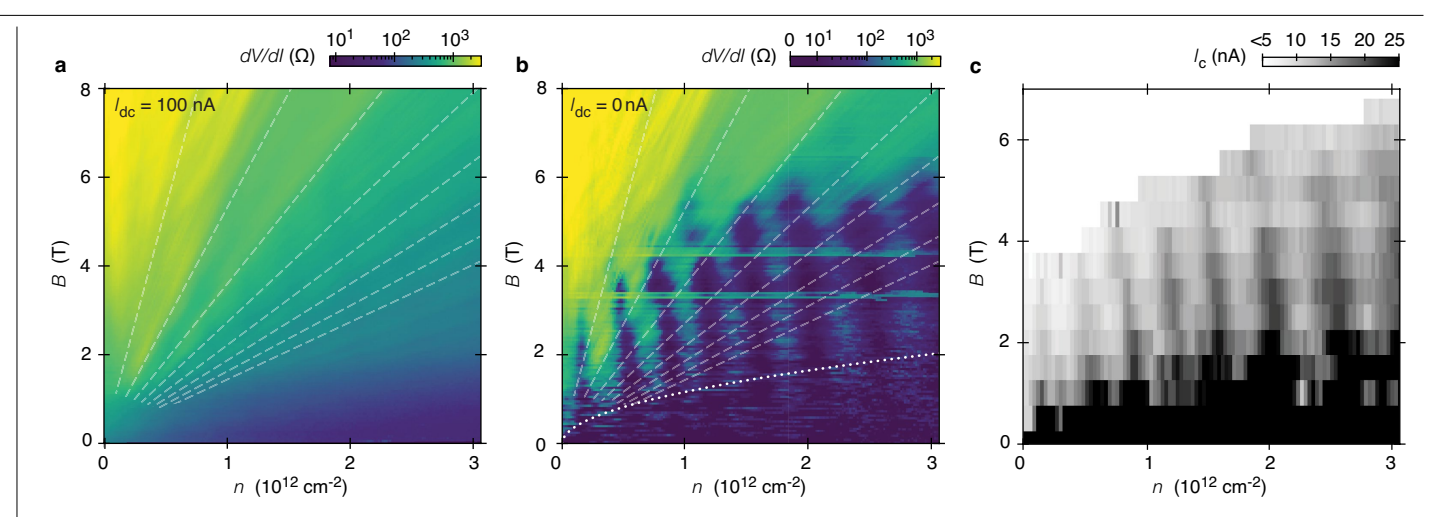
Extended Data Fig. 8 | Temperature dependence of proximity superconductivity in zero and quantizing fields. (a and c) Differential resistance maps $dV/dI(I_{dc}, T)$ at 0 and 3 T, respectively. (b and d) Examples of dV/dI for selected temperatures (cross-sections from the corresponding

maps). White dashed curve in panel a: fit to eq. S1 above 2 K. Data are for a Josephson junction with a single domain wall, $L \approx 200$ nm, $n \approx 2 \times 10^{12}$ cm⁻², $I_{\rm ac} = 5$ nA.



Extended Data Fig. 9 | **Shapiro steps in the quantum Hall regime.** (a) Voltage vs current characteristics as a function of RF power. For clarity, the curves are shifted horizontally by 10 nA each. The power P was increased in steps that corresponded to $V_{\rm rf}$ increasing from 0 to 26 μ V. Shown is the same one-domain wall junction as in Fig. 1 of the main text; $f_{\rm rf} = 3.3$ GHz, B = 3 T, no $I_{\rm ac}$ applied; $n \approx 1.8 \times 10^{12}$ cm⁻² which corresponds to a maximum in $I_{\rm c}$ (Fig. 3b of the main text). Inset: ΔV as a function of the RF frequency. Green line: $\Delta V = \phi_0 f_{\rm rf}$ as per eq. S2. (b) ${\rm d}V/{\rm d}I(I_{\rm dc})$ with varying $V_{\rm rf}$. The same junction and conditions as for

panel \mathbf{a} ; $I_{\mathrm{ac}} = 5$ nA. Color scale: indigo to yellow is 0 to 480 Ω . (c) Same as in panel **b** but for $n \approx 1.7 \times 10^{12}$ cm⁻² which corresponds to a minimum in $I_{\mathrm{c}}(n)$; $f_{\mathrm{rf}} = 3.52$ GHz. Color scale: indigo to yellow is 70 to 440 Ω . (d) Similar map for a Josephson junction with many domain walls at B = 5 T. $N_{\mathrm{DW}} = 9 \pm 2$, $L \approx 200$ nm, $W \approx 3.5$ µm, $n \approx 2.7 \times 10^{12}$ cm⁻², $f_{\mathrm{rf}} = 3.0$ GHz, $I_{\mathrm{ac}} = 2$ nA. Color scale: indigo to yellow is 0 to 70 Ω . (e) Width of Shapiro steps extracted from the map of panel **d**. The pink curves in panels **b-d** and the black curves in panel **e** are the fits by the corresponding Bessel functions as per eq. S3. For all panels, $T \approx 50$ mK.



Extended Data Fig. 10 | Fabry-Pérot oscillations in the supercurrent provided by 1D states inside domain walls. (a and **b)** Differential resistance maps at high and low dc biases, respectively. In both cases, $I_{ac} = 5$ nA. The white dashed lines indicate the filling factors $v = 4, 8, 12, \dots$ expected for Bernal bilayer graphene. The dotted curve in panel **b** indicates the quantum Hall regime

boundary, $2r_c$ = L. (c) Oscillations in the critical current. Values of I_c are obtained from IV curves that were recorded in small steps of -3×10^{10} cm⁻² in electron density and steps in B of 0.5 T. All the measurements were carried out at $T \approx 50$ mK using junctions with a single domain wall and $L \approx 200$ nm.